

Performance Predictions for Continuous Wave Mode Operation of a Rotating Magnetic Field Thruster

Christopher L. Sercel*, Tate M. Gill †, and Benjamin A. Jorns‡
University of Michigan, Ann Arbor, MI, 48109

The performance of a ~4 kW-class rotating magnetic field (RMF) thruster operating in CW-mode is analytically predicted. Scaling arguments based on a first-principles analysis are employed to translate experimental measurements of electron density, electron temperature, and current density from triple Langmuir probe and inductive probe measurements of pulsed operation into equivalent values for CW operation at the same mass flow rate and applied bias field strength. Measurements are considered from thruster operation at combinations of 45 and 60 sccm Xe and 120 and 180 G peak centerline bias field. It is predicted that while the transition to CW-mode operation would reduce power draw by ~30% while increasing efficiency by a factor of 3-5, the overall efficiency will remain below 6%. The low CW-mode performance is driven primarily by wall interactions, with the majority of thrust arising from electron pressure at the walls and the majority of thermal losses arising from electron wall losses. These results are discussed in the context of design strategies to improve performance.

I. Nomenclature

\vec{B}_0	=	Bias magnetic field
\vec{B}_{RMF}	=	Rotating magnetic field
ω	=	Rotating Magnetic Field frequency
ω_{ce}	=	Electron cyclotron frequency
f_{rep}	=	Pulse repetition rate
\vec{E}	=	Electric field
\vec{v}_e	=	Electron velocity
u_{th}	=	Thermal velocity of diffusing neutral gas
u_{cw}	=	Exhaust velocity for CW-mode operation
\vec{j}	=	Current density
I_{RMF}	=	Peak-to-peak current flowing through RMF antennas
I_s	=	DC current supplied to RMF PPU
V_s	=	Voltage supplied to RMF PPU
ν_{ei}	=	Electron-ion collision frequency
η_{ei}	=	Plasma resistivity
δ	=	Classical conductive skin depth
$\ln \Lambda$	=	Coulomb logarithm
n_e	=	Electron density
n_n	=	Neutral density
N_e	=	Total number of electrons in thruster volume
T_e, T_{eV}	=	Electron temperature
\dot{m}	=	Mass flow rate
t_p	=	Time corresponding to peak current drive
F_L	=	Lorentz force
F_{th}	=	Electron pressure force
P_{ohm}	=	Ohmic power

*PhD Candidate, Department of Aerospace Engineering, AIAA Student Member

†PhD Candidate, Department of Aerospace Engineering, AIAA Student Member

‡Associate Professor, Department of Aerospace Engineering, AIAA Associate Fellow

P_{rad}	=	Radiated power
P_{wall}	=	Power lost to electron-wall interactions
P_{Fth}	=	Jet power associated with electron pressure force
P_{FL}	=	Jet power associated with Lorentz force
P_{LL}	=	Power lost to resistance in RMF transmission lines
P_j	=	Total jet power
s	=	Relative slip between electrons and RMF
R_T	=	Temperature ratio (CW-mode to pulsed mode)
R_n	=	Density ratio (CW-mode to pulsed mode)
η_c	=	Coupling efficiency
$\eta_a\eta_p$	=	Combined plasma and acceleration efficiency
η_T	=	Total efficiency
Ω_{eff}	=	Effective RMF line resistance
x, y	=	Coordinates transverse to the thruster axis
z	=	Thruster axial Coordinate
θ	=	Thruster azimuthal coordinate
θ_C	=	Thruster cone half-angle
r	=	Thruster radial coordinate
R	=	Thruster wall radius
e	=	Electron charge
μ_0	=	Vacuum permeability
m_e	=	Electron mass
M	=	Ion, neutral mass

II. Introduction

THE Rotating Magnetic Field (RMF) thruster, a type of inductive pulsed plasma thruster (IPPT), employs a rotating magnetic field to induce azimuthal current in a plasma. This azimuthal current is leveraged to produce thrust via a Lorentz interaction with a radial applied field and secondary induced fields. The RMF thruster shares many potential advantages with other in-family pulsed plasma devices [1]. These include high throttability while maintaining efficiency and specific impulse, high specific power, [2]; and an absence of plasma-wetted electrodes[3]. The RMF current drive scheme has the additional benefit that the induced plasma current depends on the rotational frequency of the RMF rather than its magnitude [4], as is the case for other IPPTs [5]. The RMF thruster can thereby avoid the high current and voltage transients required for other IPPTs to operate. These transients make power supply design challenging, especially in light of switching circuit longevity.

Because of the RMF thruster's potential advantages, several groups have investigated the technology. Of particular note are the efforts by MSNW LLC and the University of Washington with their ELF thruster [6],[7][8], as well as the Tokyo University of Agriculture and Technology [9][10][11]. Universally, however, these groups have found the RMF efficiency to be low. The ELF thruster was reported at up to 8% efficiency, we believe this number is slightly suspect due to generous assumptions and an experimental setup involving strong magnetic fields present at the location of the ballistic pendulum used to estimate impulse. Furukawa, meanwhile, estimated ~ 7 mN thrust for 3 kW operation on 60 sccm Argon with 700 kHz RMF rotation frequency. This translates into $\sim 0.5\%$ efficiency. More recently at the University of Michigan, we made the first direct performance measurements of an RMF thruster using a thrust stand and found overall efficiency to peak at $\sim 0.5\%$ at 3 kW operation using Xe propellant between 15 and 60 sccm flow rate and 400 kHz RMF rotation frequency [12].

In an effort to uncover the mechanisms driving this poor performance, in a follow on investigation, we performed detailed plasma probing including Faraday, Langmuir, and retarding potential analyzer measurements [13][14]. In parallel, we employed inductive probing techniques to measure the effectiveness of the current drive mechanism [15]. Between these studies, we found that while the RMF has nearly 100% efficiency at coupling power into the plasma, driving near-ideal levels of azimuthal current, the poor efficiency results from prohibitively high losses stemming primarily from radiation resulting from electron-ion excitation .

In light of these previous results, one possible strategy to improve performance is to reduce the operating plasma density in the the thruster. This is because the frequency of excitation collisions scales quadratically with electron density [16]. The challenge with reducing plasma density in the thruster, however, is that in pulsed operation, the

discharge forms from a dense neutral environment. This stems from that fact that between pulses, the thruster is allowed to refill with a nearly constant density field of neutrals. When the discharge ignited, this entire volume is ionized and excited simultaneously leading to the high excitation losses. As an alternative, if the thruster were instead operated in a continuous wave (CW) -mode at the same mass flow rate of propellant, the RMF Lorentz force would accelerate the ions continuously through the thruster. This acceleration in turn would lower the density throughout the volume, thus reducing excitation losses. In principle then, a CW-mode RMF thruster would retain its strengths as a high specific-power, ISRU-compatible device while mitigating its main loss mechanism. In light of this potential tradeoff, the need is apparent for an investigation into the effectiveness of CW-mode operation for an RMF thruster.

As a path finding effort to inform such a study, the goal of this work is to provide performance predictions for CW-mode operation using scaling arguments and extrapolations from previous measurements from pulsed mode operation. This paper is organized in the following way. In Section III, we discuss the presently understood principles of operation for the RMF thruster. In Section V, we overview the approach by which we attempt to translate pulsed data into CW results. We show our results in Section VI and discuss their implications in Section VII.

III. Principles of Operation

We begin this section by establishing the presently understood principles of operation for the RMF thruster before following with an explanation of the probe technology used in this study.

As shown in Figure 1, the canonical geometry of the RMF thruster consists of a plasma-bounding cone surrounded by a pair of saddle coils that produce the RMF and one or more DC electromagnets that provide a steady bias magnetic field. A seed plasma source positioned at the smaller 'throat' end of the cone generates a plasma that flows toward the exit plane. Each saddle coil is shaped such that it effectively forms a Helmholtz pair with itself, with each loop on the opposite side of the cone. In this way, running a current through one of the saddle coils produces a near-uniform magnetic field orthogonal to the cone axis. By orienting each saddle coil 90 degrees from the other and running sinusoidal current through each coil 90 degrees out of phase from the other, their magnetic fields can be superposed to result in a field transverse to the axis of the cone whose direction rotates with the same frequency as the input current sine waves. The magnitudes of the current through each electromagnet are tuned to produce field shape such that the field is tangent to the plasma-bounding cone along the walls. This in principles help improve plasma confinement during plasma generation and acceleration.

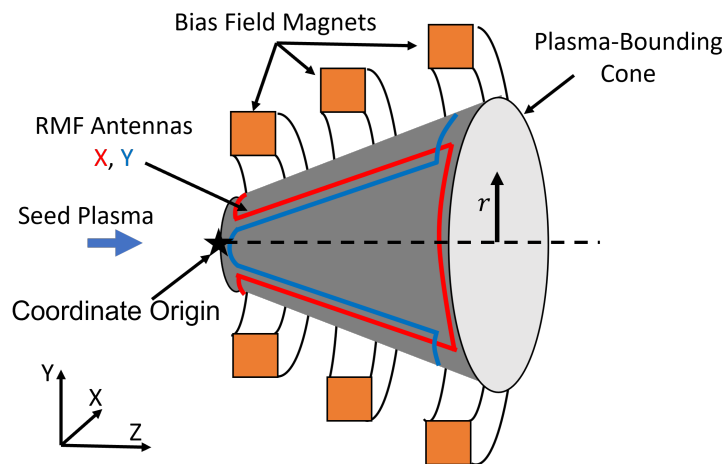


Fig. 1 Basic geometry of the canonical RMF thruster.

A. Current Induction

The rotating magnetic field in the thruster can be described by

$$\vec{B}_{RMF} = |B_{RMF}| (\cos(\omega t)\hat{x} + \sin(\omega t)\hat{y}), \quad (1)$$

where ω is the RMF frequency and the coordinates x and y match the convention established in Figure 1. Applying Faraday's Law to this expression results in an induced axial electric field:

$$\vec{E} = \omega |B_{RMF}| (x \cos(\omega t) + y \sin(\omega t)) \hat{z}. \quad (2)$$

For the simplest case, we assume the cone is already filled with a plasma of non-inertial, collisionless electrons and cold, unmagnetized ions. For these conditions, the generalized Ohm's Law reduces to the form

$$\vec{E} = -\vec{v}_e \times \vec{B}, \quad (3)$$

where \vec{v}_e is electron velocity. Substituting Equations 1 and 2 into Ohm's law, we find that the electron velocity is given by

$$\vec{v}_e = \omega (-y\hat{x} + x\hat{y}) = \omega r \hat{\theta}. \quad (4)$$

We thus arrive at an approximation for the current density:

$$\vec{j} = -en_e \omega r \hat{\theta}. \quad (5)$$

where r refers to the radial coordinate. Significantly, we note that j does not depend on the magnitude of B , which is a potential advantage (Section II of this current generation mechanism compared to other pulsed inductive devices. In reality, induced currents, collisionality, and thermal effects combine to screen out the RMF and thus change \vec{B}_{RMF} from its ideal form in Eq. 1. To combat this, so-called penetration requirements have been proposed which establish the minimum RMF field strength required to keep Eq. 5 approximately valid [17]. The penetration limit requires that

$$\left(\frac{v_{ei}}{\omega_{ce}}\right)^2 \left(\frac{R}{\delta}\right)^2 \ll 1 \quad (6)$$

where v_{ei} is electron-ion collision frequency, R is the radius of the thruster, ω_{ce} is the electron cyclotron frequency with the RMF, and δ is the classical skin-depth of the plasma at the RMF frequency. To re-casting these quantities in terms of thruster operational parameters, we make several simplifying assumptions. First, we take the Xenon collision frequency fit from Goebel and Katz [16], which states

$$v_{ei} = \left(2.9 \times 10^{-12}\right) \frac{n_e \ln \Lambda}{T_{eV}^{\frac{3}{2}}} \quad (7)$$

where the constant scalar is a species-specific fit parameter, T_{eV} refers to the electron temperature in units of electron-volts, and $\ln \Lambda$ refers to the Coulomb logarithm, given by

$$\ln \Lambda = 23 - \frac{1}{2} \ln \left(\frac{10^{-6} n_e}{T_{eV}^3}\right). \quad (8)$$

We further note that $\omega_{ce} = \frac{eB_{RMF}}{m_e}$ where B_{RMF} refers to the magnitude of the RMF field. Taking each antenna as forming a Helmholtz pair with itself with radius approximately $\frac{1}{\sqrt{3}}$ smaller than the thruster cone at any given axial location, we find the RMF magnitude to be

$$B_{RMF} = \left(\frac{4}{5}\right)^{\frac{2}{3}} \frac{\mu_0 I_{RMF}}{R_{antenna}} \quad (9)$$

$$B_{RMF} = \sqrt{3} \left(\frac{4}{5}\right)^{\frac{2}{3}} \frac{\mu_0 I_{RMF}}{R} \quad (10)$$

where R refers to the radius of the thruster at any particular axial location. Finally, we use the definition of classical skin depth for δ

$$\delta = \sqrt{\frac{2\eta_{ei}}{\mu_0}} \omega \quad (11)$$

where $\eta_{ei} = \frac{m_e \nu_{ei}}{e^2 n_e}$ is the resistivity of the plasma. Substituting these expressions into Eqn. 6 and simplifying results in the requirement that

$$I_{RMF} \gg 3.15 \times 10^{-19} (\ln \Lambda)^{\frac{1}{2}} R^2 n_e T_e^{-\frac{3}{4}} \omega^{\frac{1}{2}}. \quad (12)$$

While this expression has limited utility for choosing a specific value of I_{RMF} to use owing to its nature as a 'much greater than' condition, it allows us to examine the scaling for penetration requirements for the same device as operating conditions change. We note that the denser the plasma, the easier it is for surface currents to 'screen out' the RMF, that an RMF with a faster rotational frequency is easier to screen out, and that hotter (more mobile) electrons will reduce the effectiveness of the screening effect. Additionally, while this analysis assumes plasma is already present in the thruster before the RMF is pulsed, the RMF is a prolific ionizer and this process requires only a seed plasma. In our case, a LaB₆ hollow cathode produces a seed plasma of roughly 1-3% overall ionization fraction before the RMF is pulsed.

B. Thrust

Lorentz force-based thrust arises from the interaction of the azimuthal induced plasma current and the radial component of the magnetic field according to

$$F_L = \iiint_V B_{0,r} j_{\theta} d^3r + \iiint_V B_{struct,r} j_{\theta} d^3r, \quad (13)$$

where V refers to the space wherever plasma exists, the magnetic field B is the combination of the applied steady bias field, B_0 , and the so-called structure field B_{struct} . This latter field results from transient secondary currents which are induced in nearby conductive structural elements by virtue of the rapid onset of plasma current [15]. Because of its transient nature, we note that while the structure field force is significant in pulsed-mode operation, it will necessarily be zero during CW-mode operation. We also identify that thrust may occur due to pressure effects from wall interactions. Considering a control volume whose walls include the inlet area of the thruster cone, the walls of the thruster cone, and extend out into the plume to where density falls to zero, this thermal force is given by

$$F_{th} = \iint_{wall} n_e k_B T_e d\vec{A} + \iint_{inlet} n_e k_B T_e d\vec{A} + \iint_{plume} n_e k_B T_e d\vec{A} \quad (14)$$

$$F_{th} = \iint_{wall} n_e k_B T_e d\vec{A} \quad (15)$$

$$F_{th} = 2\pi \sin(\theta_c) \int n_e k_B T_e r d\vec{l} \quad (16)$$

where the electron pressure $n_e k_B T_e$ is integrated over the surface of the control volume, θ_c is the half-angle the thruster cone makes with respect to the axis, r is the radial coordinate along the walls, and $d\vec{l}$ is the unit length along the wall of the cone. We note that we have neglected pressure effects at the inlet to the cone where electron density and temperature due to lack of ionization. We also consider that the density will eventually fall to zero in the plume and thus the area corresponding to the exit plan should not contribute to force.

IV. Experimental Setup

In this section, we describe the experimental setup and operating conditions used to collect the pulsed-mode data.

A. Probes

We omit a detailed description of the probe methodology for Bdot probes used to measure induced plasma current or triple Langmuir probes used to measure electron density and temperature as these topics are discussed in detail in

Sercel et al., 2022 [15] and Gill et al., 2022 [14], respectively. However, we present here a brief overview of the probing technologies used and what information can be gleaned from them.

Both types of probe were mounted on a two-axis motion stage and moved throughout the horizontal plane inside the thruster to take spatially- and temporally-resolved measurements throughout the cone.

1. Triple Langmuir Probing

Triple langmuir probing was used to measure electron density and temperature, both of which are critical for determining electron pressure force, electron wall losses, radiation losses, and necessary RMF current to maintain penetration – all of which play a role in the analysis described in Section V. Representative data for electron number and temperature are shown in Figure 5. The triple Langmuir probe (TLP) consists of three separate tungsten probes inserted into the plasma. A voltage V_{d3} is enforced between probes 1 and 3, while probe 2 is allowed to float. The electron temperature can be expressed implicitly as a function of V_{d3} and $V_{d2} = V_1 - V_2$, the difference in voltage between probes 1 and 2. This takes the form

$$\frac{1 - \exp\left(-\frac{V_{d2}}{T_{eV}}\right)}{1 - \exp\left(-\frac{V_{d3}}{T_{eV}}\right)} = \frac{1}{2} \quad (17)$$

Using orbital motion-limited (OML) theory for expansion of the ion sheath, the electron density can also be determined via the relation

$$n_e = \frac{1}{\alpha(T_{eV})} \left[\beta(V_3) - \beta(V_2) \exp\left(\frac{V_{d2} - V_{d3}}{T_{eV}}\right) \right] \quad (18)$$

where α and β are given by

$$\alpha = \frac{eA_p}{\pi} \quad (19)$$

$$\beta = \sqrt{\frac{2e(-V)}{M_i}} \quad (20)$$

where A_p is the area of the probe, and M_i is the ion mass. The major strength of the TLP is that, through Eqns. 17 and 18, the density and temperature of the electrons can be measured instantaneously without the need to sweep over a voltage range as in a traditional Langmuir probe. This is invaluable for measurements in pulsed devices where it is not reasonable to perform a Langmuir sweep on a short enough timescale to properly assess the time-dependent physics.

2. Bdot Probing

The Bdot probe is used to directly measure changing magnetic fields, but can be extended to measure induced current density as well. Representative current data is shown in Figure 3. This is critical to establish effectiveness of the RMF current drive mechanism, as well as to calculate the Lorentz force present in the plasma at any given time. The Bdot probe consists of a wire loop (or small bobbin of many loops) situated with its axis parallel to the field to be measured. According to Faraday's Law, the voltage induced on a circuit owing to a change in magnetic flux is given as

$$V_p = -\frac{d\Phi}{dt} \quad (21)$$

$$V_p \approx -A_p N_p \frac{\partial B}{\partial t} \quad (22)$$

where Φ is the magnetic flux through the probe, A_p is the area of a wire loop on the probe bobbin, N_p is the number of loops on the bobbin, and B is the changing magnetic field. In reality, this requires a frequency-dependent calibration process owing to non-idea circuit effects. This calibration is performed by placing the probe in a magnetic field of

known amplitude and frequency and measuring the voltage response across a range of such frequencies to develop a calibration transfer function $\beta(\omega_s)$, where ω_s refers to the signal frequency content, such that

$$B(t) = \int \text{IFFT} \left(\frac{\text{FFT}(V_p)}{\beta(\omega_s)} \right) dt \quad (23)$$

In this study, a two-axis Bdot probe, constructed by mounting two Bdot probes orthogonally, was used to measure B_r and B_z in the thruster simultaneously. By Ampere's Law,

$$\vec{j} = \vec{\nabla} \times \vec{B} \quad (24)$$

$$j_\theta = \frac{\partial B_z}{\partial r} - \frac{\partial B_r}{\partial z} \quad (25)$$

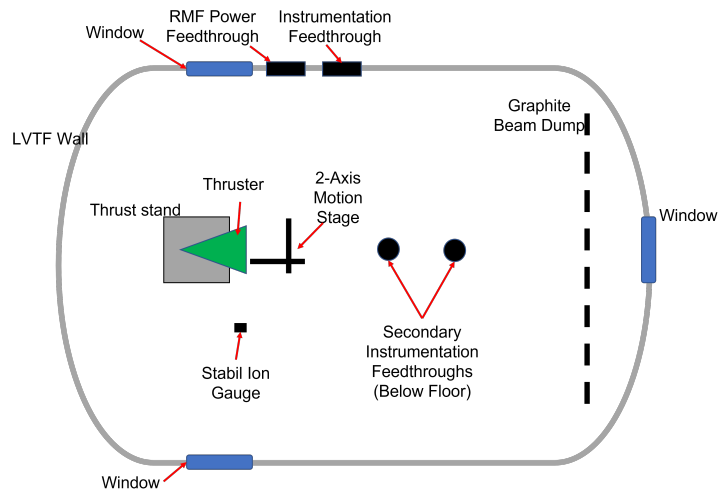
where j_θ is the plasma current density in the azimuthal direction.

B. PEPL RMFv2 Thruster

The design methodology behind the unit under test, known as the PEPL RMFv2, is discussed in detail in Sercel et al., 2021 [12]. Briefly, however, the thruster consists of a cone constructed from mica, a dielectric, mounted on a scaffold of fiberglass. The cone is 33 cm in length and has an exit radius of 10 cm. A LaB_6 hollow cathode, chosen due to institutional familiarity rather than fidelity to a flight-like design, flows partially-ionized Xe propellant into the upstream opening of the cone, and a neutral injector to provide additional propellant flow is situated at the ext oriented backward. Three electromagnets are used to produce the bias magnetic field.



(a)



(b)

Fig. 2 Overview of the test setup in the Large Vacuum Test Facility at the University of Michigan. a) Photograph of the PEPL RMFv2 on its thrust stand. b) Top-down diagram of chamber configuration.

RMF antennas consist of copper tubing bent into shape to produce the proper Helmholtz field shape. To generate the oscillating current, each antenna is paired with a tuning capacitor bank to form a series LC circuit whose resonant frequency determines the RMF frequency. Energy from a large backing capacitor bank is pulsed at the resonant frequency of the LC circuits to produce large currents.

C. Test Facility

We performed our measurements in the Large Vacuum Test Facility at the University of Michigan. This is a 6×9 m chamber capable of xenon cryopumping speeds up to 6×10^5 L/s [18]. Not every pump was used during these tests, resulting in facility base pressures of $\sim 2 \times 10^{-7}$ Torr and operating pressures of $\sim 5 \times 10^{-6}$ Torr-xenon as measured by a Stabil ion gauge positioned according to electric propulsion community best practices [19]. The thruster was located approximately 3 meters from a graphite beam dump. Feedthroughs provided high power connections to conduct current to the RMF antennas as well as device diagnostics. Pearson 110 current monitors were used to measure injected RMF current. Viewports allowed for access by both conventional cameras and high speed video at 50 kHz to monitor thruster operation.

D. Operating Points

The RMF thruster has several operational variables which can be adjusted parametrically to change thruster behavior without any physical reconfiguration. All the direct experimental measurements used in this work were taken at 2 kA pk-pk RMF current and 125 μ s pulse duration. Steady flow rate and peak centerline bias magnetic field strength were adjusted to produce the combinations 45 sccm Xe/120 G, 45 sccm Xe/180 G, and 60 sccm Xe/180 G.

V. Analysis Methodology

In this section, we outline scaling arguments for relating transient measurements from pulsed operation to predictions for plasma properties behavior during CW-mode operation. We then translate these relationships to estimates for performance.

A. Relating Pulsed-Mode Measurements to CW-Mode Quantities

1. Mass Conservation

Figures 3a and 3b show the total current induced in the thruster as a function of time for the 45 sccm Xe, 2 kA pk-pk RMF current amplitude, 180 G peak centerline bias condition for 125 μ s and 200 μ s cases. These figures illustrate a key trend in all data taken. There first is a low signal followed by an ionization event when the entire volume of the thruster is ionized. High levels of current are then driven before electron density and current density fall off as plasma is ejected from the thruster.

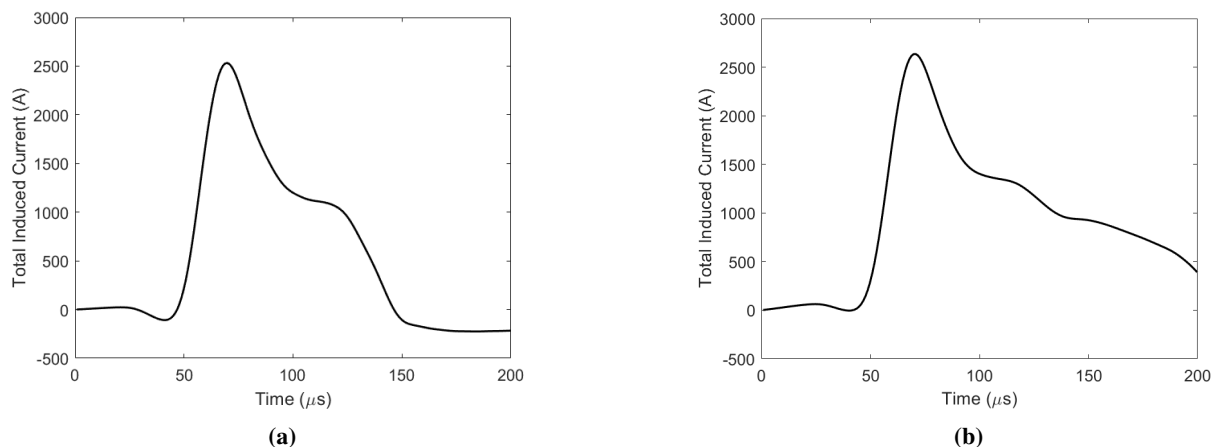


Fig. 3 Total current driven at the 45 sccm Xe, 2 kA pk-pk RMF current amplitude, 180 G peak bias field condition. a) 125 μ s pulse duration. b) 200 μ s pulse duration.

The high peak currents during the initial ionization event can be ascribed to the initial condition in the thruster immediately before the pulse. Because propellant flow rate is steady and the time between pulses long compared to the fill time, the pre-pulse neutral density in the thruster is dictated by the thermal speed of the neutrals according to mass

continuity:

$$\dot{m} = Mn_n(z)A_c(z)u_{th}, \quad (26)$$

where M is the mass of a propellant atom, $u_{th} = \sqrt{\frac{8k_B T_n}{\pi M}}$, A_c is the local cross section of the cone, and n_n is the neutral density. Because of the density scaling for induced current density described in Eqn. 5, this leads to the very high initial current peak.

As plasma is ejected from the cone and density drops from initial levels closer to steady-state levels, plasma current drops. However, although Figure 3b helps to show this trend, the pulse is not long enough to have measured the steady value of current as the value is still dropping at the end of the 200 μ s pulse. To attempt to quantify the CW-mode density values, we make two major assumptions.

First, we assume that the electron distribution at the time corresponding to the peak of the driven current plot in Figure 3a is equal to the neutral density distribution pre-pulse. This is equivalent to stating that every neutral atom is singly ionized and the distribution does not change immediately as a result of that ionization process. In analytic form, this can be written

$$n_n(t < 0) = n_e(t = t_p). \quad (27)$$

where t_p refers to the time at which the current peaks during the pulse, and the pulse begins at $t = 0$. Next, we make the further assumption that although the total number of electrons may change between the peak of the initial pulse and the CW-mode value, the shape of the distribution does not. Put mathematically, this says

$$\frac{n_e(t = t_p)}{\iiint_V n_e(t = t_p) dV} = \frac{n_e(t \gg t_p)}{\iiint_V n_e(t \gg t_p) dV} \quad (28)$$

Next we note that because we have assumed full single ionization, and taking into account quasi-neutrality which states that $n_e = n_i$ at any given time and location, where n_i is the ion density, we define

$$n_p = n_e(t = t_p) = n_i(t = t_p) \quad (29)$$

$$n_{cw} = n_e(t \gg t_p) = n_i(t \gg t_p) \quad (30)$$

We can finally call upon conservation of mass, which states

$$\dot{m} = Mn_p(z)A_c(z)u_{th} = Mn_{cw}(z)A_c(z)u_{cw}(z) \quad (31)$$

$$u_{cw} = \frac{n_p(z)}{n_{cw}(z)}u_{th} \quad (32)$$

$$u_{cw} = R_n u_{th} \quad (33)$$

where u_{cw} is the exit velocity of the ions in CW-mode operation and where we have defined $R_n = \frac{n_p(z)}{n_{cw}(z)}$ to be the density ratio between the peak of the pulse and CW-mode operation. Eqn. 33 states two things. First, the lower the density due to CW-mode operation relative to that dictated by thermal diffusion, the higher the CW-mode exhaust velocity will be. Second, because n_p and n_{cw} are assumed to have the same profile, their quotient is a scalar constant, and thus u_{cw} is assumed not to be a function of position in the cone.

2. Momentum Conservation

While u_{th} is a quantity easily calculated and n_p is measured, Eqn. 33 is not closed. To remedy this, we add momentum conservation, which states that

$$\iint Mn\vec{u}(\vec{u} \cdot \vec{dA}) = F \quad (34)$$

where F is the sum of all external forces on the fluid. In this case, we take the forces to include the Lorentz force owing to the bias field and thermal force owing to electron pressure on the thruster walls. We further assume that all velocity is directed axially. Eqn. 34 then simplifies to

$$Mn_{cw,exit}A_{exit}u_{cw}^2 - Mn_{th,in}A_{in}u_{th}^2 = F_{L,cw} + F_{th,cw} \quad (35)$$

$$\dot{m}(u_{cw} - u_{th}) = \iiint_V B_{0,r}j_{cw}d^3r + 2\pi \sin(\theta_c) \int n_e k_B T_e r \vec{dl} \quad (36)$$

$$(37)$$

where we have recognized $\dot{m} = MnAu$ for both CW and pulsed values, and substituted the expressions for Lorentz and thermal force from Eqns. 13 and 16.

To determine the induced current density j_{cw} , we consider that the ideal current density is given by $j = en_e\omega r$. Taking inspiration from standard analysis techniques for induction motors, which function on the same principles as the RMF current drive, we define a slip $s(\vec{r}, t)$ to account for difference in rotational speeds between the electrons and the RMF caused by lack of full penetration. In this way,

$$s(\vec{r}, t) = \frac{\omega - \omega_e(\vec{r}, t)}{\omega} \quad (38)$$

where ω without a subscript again refers to the RMF frequency, and ω_e is the rotational frequency of the electrons residing at location $vecr$ and time t . For reference, the slip measured in the 45 sccm, 2 kA RMF current, 180 G, 125 μ s case is averaged over the volume of the cone and plotted over time in Figure 4.

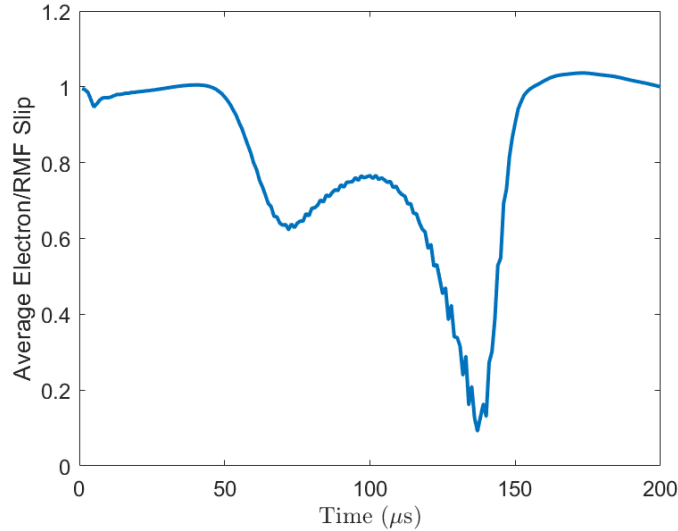


Fig. 4 Electron slip, averaged over the volume of the thruster, for the 45 sccm, 2 kA pk-pk RMF current, 180 G centerline bias field, 125 μ s condition.

The slip is observed as high initially while electron density is near zero, then drops as the initial ionization event allows currents to form in the dense initial plasma before dropping further as the plasma is ejected until the end of the pulse. We note that we should not expect the slip to remain constant throughout the pulse, as the RMF current remains constant at 2 kA pk-pk but the electron density changes significantly, thus dynamically changing the penetration condition set forth in Eqn. 12. With this being said, we make the next major assumption in this analysis, that we preserve the same slip between the peak pulse value (~ 0.6 in this case) and the CW-mode value. This would necessarily require the same degree of penetration. In other words,

$$\frac{I_{RMF,p}}{I_{RMF,p,min}} = \frac{I_{RMF,cw}}{I_{RMF,cw,min}} \quad (39)$$

$$\Rightarrow I_{RMF,cw} \approx \frac{n_{cw}}{n_p} \left(\frac{T_{cw}}{T_p} \right)^{-\frac{3}{4}} I_{RMF,p} \quad (40)$$

where $I_{RMF,min}$ is calculated by considering Eqn. 12 as an equality, and the \approx sign is used due to the influence of the Coulomb logarithm in Eqn. 12. However, as the Coulomb logarithm is highly insensitive to changes in density and temperature, the rough equality holds.

Given the introduction of the slip term, we therefore modify Eqn. 5 to become

$$j = ens\omega r. \quad (41)$$

Given our assumption that CW-mode slip and pulse peak slip are equal, and leveraging Eqn. 41, we find

$$\frac{j_{cw}}{j_p} = \frac{n_{cw}}{N_p} \quad (42)$$

$$\Rightarrow j_{cw} = R_n j_p. \quad (43)$$

Substituting Eqn. 43 into 36 and defining $R_T = \frac{T_{cw}}{T_p}$, we find

$$\dot{m} (u_{cw} - u_{th}) = R_n \iiint_V B_{0,r} j_p d^3 r + R_n R_T \iint_A n_p k_B T_{e,p} \sin \theta_c dA. \quad (44)$$

This equation states that forces owing to Lorentz interaction and electron thermal pressure will directly lead to an increase in exit velocity for CW-mode operation relative to the input diffusion velocity. Further, it states that this effect will be reduced linearly with CW-mode density for both effects, and reduced with CW-mode temperature for the pressure force. However, we have introduced a new unknown variable R_T , which will require a third equation to close the system.

3. Energy Conservation

The thermal force in Eqn. 44 introduces electron temperature, requiring the addition of an energy equation to close the system. In the CW-mode, the system must necessarily be at steady state, therefore $\frac{dE_{cw}}{dt} = 0$. Further, we assume that the sole heat generation mechanism is ohmic heating due to classical collisions and that thermal energy is lost due to radiation from excitation collisions, electron wall losses, and the power associated with the thermal force defined in Eqn. 16. Therefore,

$$P_{ohm,cw} + P_{ind,cw} - P_{rad,cw} - P_{wall,cw} - P_{Fth,cw} - P_{FL,cw} = 0 \quad (45)$$

$$P_{ohm,cw} = P_{rad,cw} + P_{wall,cw} + P_{Fth,cw} \quad (46)$$

where $P_{ohm,cw}$ is thermal power generated through ohmic heating, $P_{ind,cw}$ is the inductive power introduced to the system by the RMF, $P_{rad,cw}$ is the radiated power lost via excitation collisions, $P_{wall,cw}$ is the power lost to electron-wall interactions, $P_{Fth,cw}$ is the power associated with accelerating propellant via electron pressure force, and $P_{FL,cw}$ is the power associated with accelerating propellant via the Lorentz force. We make the assumption that all inductive power introduced is used to accelerating propellant via the Lorentz force, so that $P_{ind,cw} = P_{FL,cw}$. We then seek functional forms for each of the remaining terms. Ohmic power will be given by the expression

$$P_{ohm} = \iiint_V \eta_{ei} j^2 dV \quad (47)$$

where plasma resistivity $\eta_{ei} = \frac{m_e v_{ei}}{e^2 n_e}$ and v_{ei} is given in Eqn. 7. Substituting plasma resistivity into Eqn. 47, we find

$$P_{ohm} = \iiint_V \left(2.9 \times 10^{-12}\right) \frac{m_e}{e^2} \ln \Lambda T_{eV}^{-\frac{3}{2}} j^2 dV \quad (48)$$

$$\Rightarrow P_{ohm,cw} = R_n^2 R_T^{-\frac{3}{2}} \iiint_V \left(2.9 \times 10^{-12}\right) \frac{m_e}{e^2} \ln \Lambda_{cw} T_{eV,p}^{-\frac{3}{2}} j^2 dV \quad (49)$$

where electron-ion collision frequency is taken from Goebel and Katz [16], $\ln \Lambda$ is the Coulomb logarithm, given as $\ln \Lambda = 23 - \frac{1}{2} \ln \left(10^{-6} n_e T_{eV}^{-\frac{3}{2}}\right)$, and T_{eV} refers to electron temperature in units of electron Volts.

Radiated power is calculated using the expression

$$P_{rad} = \iiint_V n^2 \sigma^* v_e \epsilon^* dV \quad (50)$$

$$P_{rad,cw} = R_n^2 R_T^{\frac{1}{2}} \iiint_V n_p^2 \sigma^* \sqrt{\frac{8k_B T_p}{\pi m_e}} \epsilon^* dV \quad (51)$$

where $\langle \sigma^* \rangle$ is the electron-ion excitation collision cross section, taken from a numerical fit by Mikellides et al. [20], v_e is mean electron velocity, and ϵ^* is the energy released per excitation collision, taken from Hayashi et al. to be 8.32 eV [21][22].

Electron power loss to the walls of the device are taken from Goebel and Katz [16] and simplified to

$$P_{wall} = \iint_A \sqrt{\frac{e^3}{2\pi m_e}} \left(2 + \sqrt{\frac{2M_i}{\pi m_e}}\right) \exp\left(-\sqrt{\frac{2M_i}{\pi m_e}}\right) n T_{eV}^{\frac{3}{2}} dA \quad (52)$$

$$P_{wall,cw} = R_n R_T^{\frac{3}{2}} \iint_A \sqrt{\frac{e^3}{2\pi m_e}} \left(2 + \sqrt{\frac{2M_i}{\pi m_e}}\right) \exp\left(-\sqrt{\frac{2M_i}{\pi m_e}}\right) n_p T_{eV,p}^{\frac{3}{2}} dA \quad (53)$$

Finally, power due to thermal acceleration by means of pressure at the thruster wall is given by

$$P_{Fth} = u F_{th} \quad (54)$$

$$P_{Fth} = u_{cw} R_n R_T \iint_A n_p k_B T_p \sin \theta_c dA \quad (55)$$

$$P_{Fth} = u_{th} R_n^2 R_T \iint_A n_p k_B T_p \sin \theta_c dA \quad (56)$$

Substituting Eqns. 49,51,53,56 into 46 and making the proper substitutions, we find

$$\begin{aligned} R_T^{-\frac{3}{2}} \iiint_V \left(2.9 \times 10^{-12}\right) \frac{m_e}{e^2} \ln \Lambda_{cw} T_{p,eV}^{-\frac{3}{2}} dV &= R_n^2 R_T^{\frac{1}{2}} \iiint_V n_p^2 \sigma^* \sqrt{\frac{8e T_{eV,p}}{\pi m_e}} \epsilon^* dV + \dots \\ \dots + R_n R_T^{\frac{3}{2}} \iint_A \sqrt{\frac{e^3}{2\pi m_e}} \left(2 + \sqrt{\frac{2M_i}{\pi m_e}}\right) \exp\left(-\sqrt{\frac{2M_i}{\pi m_e}}\right) n_p T_{eV,p}^{\frac{3}{2}} dA &+ u_{th} R_n^2 R_T \iint_A n_p k_B T_p \sin \theta_c dA \end{aligned} \quad (57)$$

where $\ln \Lambda_{cw}$ refers to the Coulomb logarithm evaluated with $T_{cw} = R_T T_p$ and $n_{cw} = R_n n_p$.

Finally, u_{cw} , R_n , and R_T can be calculated by solving the system of equations comprised of Eqns. 33, 44, and 57.

B. Performance Estimation

Once u_{cw} , R_n , and R_T are known, force can be calculated using Eqn. 44, and useful jet power with

$$P_{j,cw} = \frac{F_{cw}^2}{2\dot{m}}. \quad (58)$$

Using the framework set forth in Gill et al., 2022 [13], we can approximate the efficiency of the RMF thruster as

$$\eta_T = \eta_c \eta_a \eta_p \quad (59)$$

where η_c refers to the coupling efficiency, the fraction of energy coupled from the RMF antennas into the plasma, and η_a and η_p are the acceleration and plasma efficiencies whose product describes the ratio of coupled energy to useful directed kinetic energy. In this way, we can write

$$\eta_a \eta_p = \frac{P_{j,cw}}{P_{j,cw} + P_{rad,cw} + P_{wall,cw}}, \quad (60)$$

all quantities other than $P_{j,cw}$ are calculated in Eqn. 57. Meanwhile, the coupling efficiency will be given by

$$\eta_c = \frac{P_{j,cw} + P_{rad,cw} + P_{wall,cw}}{P_{in}} \quad (61)$$

$$\eta_c = \frac{P_{j,cw} + P_{rad,cw} + P_{wall,cw}}{P_{LL} + P_{j,cw} + P_{rad,cw} + P_{wall,cw}} \quad (62)$$

where P_{in} is the total power injected and is equal to the sum of power coupled into the plasma and P_{LL} , power lost in the RMF transmission lines. To estimate P_{LL} , we consider that we have already made the assumption that we have the same degree of penetration in the CW-mode as the pulsed mode which gives an estimate for the required RMF current via Eqn. 40. We calculate an effective RMF line resistance by comparing energy expended in a so-called 'vacuum shot' in which the RMF is pulsed at representative amplitude with no plasma present. The energy input from the main power supply can then be compared to the energy expended in the switching circuitry and RMF lines according to

$$\Omega_{eff} = \frac{I_s V_s}{f_{rep} \left(\int I_{RMF,x}^2 dt + \int I_{RMF,y}^2 dt \right)} \quad (63)$$

where we have used Ω_{eff} for the effective line resistance to avoid confusion with R_n and R_T , I_s and V_s are the voltage and current output of the feed supply, f_{rep} is the pulse repetition rate, and $I_{RMF,x}$ and $I_{RMF,y}$ are the current through the x and y RMF antennas, respectively.

Once $\Omega_{eff,cw}$ is known, we can calculate line loss by considering that the RMF current forms a sin wave. Because the average of $\sin^2(x)$ is $\frac{1}{2}$, then

$$P_{LL} = 2 \left(\frac{1}{2} \Omega_{eff,cw} I_{RMF,cw}^2 \right) \quad (64)$$

where the factor of 2 comes from having two separate and equal current paths comprising the x and y antennas. We note that in the event E_s is indeed linear with I_{RMF} , P_{LL} can then be substituted into Eqn. 62 to close the last unknown term in the performance analysis.

C. Pulse-End Measurements

In addition to the above analysis to predict CW-mode performance, we can employ measurements from the end of the pulse of the 200 μs pulse duration condition to prove sanity checks.

Figure 5 shows the total integrated electron number and average electron temperature over time using electron density measured with the TLP for a 200 μs pulse duration case. It can be seen that both plots reach a high peak, similar to the total current shown in Figure 3b which corresponds to the same operating condition. Unlike the current, however,

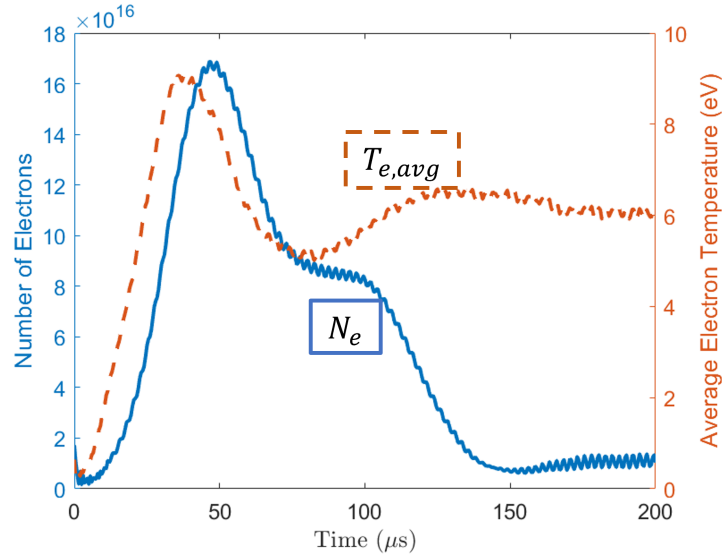


Fig. 5 Total integrated electron number N_e and averaged electron temperature $T_{e,avg}$ for the 45 sccm, 2000 A pk-pk RMF current, 180 G centerline, 200 μ s pulse duration condition

Flow Rate (sccm Xe)	Peak Bias Field Strength (G)	T_{cw} (mN)	$I_{sp,cw}$ (s)	P_{in} (kW)	$\eta_a\eta_p$	η_c	η_T
60	180	21.3	390	2.75	.042	.356	.015
45	120	19.6	474	2.46	.051	.351	.018
45	180	19.0	460	2.70	.060	.255	.015
45**	180**	35.7	824	2.35	.082	.751	.061

Table 1 Summary of results of CW-mode prediction analysis. All estimates are based on data taken from thruster operation using 2 kA pk-pk RMF current rotating at 415 kHz. The final case (set off with asterisks) is a direct measurement taken at the end of a 200 μ s pulse.

these quantities appear to find steady values at the end of the pulse while the current is still dropping at that time step. Recognizing that because the current is still dropping, this does not truly correspond to CW-mode operation, we can use the data at the 200 μ s point as a proxy for the true measurement as a means of rough validation for this analysis.

Taking the data for n_e , T_e , and j for $t = 200 \mu$ s, we calculate the Lorentz and thermal forces using Eqns. 13 (neglecting B_{struct}) and 16. Loss mechanisms are calculated in the same manner as for the CW analysis but using the directly-measured values rather than predicted CW-mode values for n_e , T_e , F_L , u , and F_{th} .

VI. Results

In this section we present the results of the analysis detailed in Section V. For each operating point, the anticipated thrust, I_{sp} , total input power, and efficiency are displayed in Table 1.

For each operating condition, CW-mode efficiency is seen to more than triple over direct measurement made in pulsed mode at the same operating conditions, where the highest measured overall efficiency is $\sim 0.5\%$ corresponding to the 45 sccm, 2 kA I_{RMF} , 180 G centerline, 125 μ s pulse condition whose CW-mode equivalent is the second entry in Table 1. This efficiency However, despite this relative uplift, overall efficiency remains low ($< 2\%$) with the $\eta_a\eta_p$ term dominating in all three conditions.

Examining the 200 μ s pulse-end measurement shown as the last entry in Table 1, thrust and specific impulse are both roughly double the corresponding values for the CW-mode prediction of the same operating condition while using $\sim 13\%$ less power. Additionally, while $\eta_a\eta_p$ is only $\sim 30\%$ higher than the CW-mode prediction, η_c is increased by a factor of 3. This result is likely erroneous, as the predicted I_{RMF} for this condition is only ~ 7 A, a number which appears unrealistically low.

To examine how the efficiency trades between pulsed-mode operation, CW-mode operation, and the pulse-end measurements which appear to lie somewhere in the transition region, we plot the relative radiation and wall losses for each case in Figure 6a. The trend exhibited agrees with the initial goal of CW-mode operation: to lower radiation losses by reducing plasma density. The calculations which refer to the peak of the pulse show radiation vastly dominating over wall losses, while the CW-mode prediction shows radiation losses to now be insignificant when compared to wall losses. The 200 μs pulse-end condition appears to correspond to a case in which the density has yet to fully reach the CW-mode state as the portion of losses relating to radiation lies between the pulse peak and CW-mode conditions.

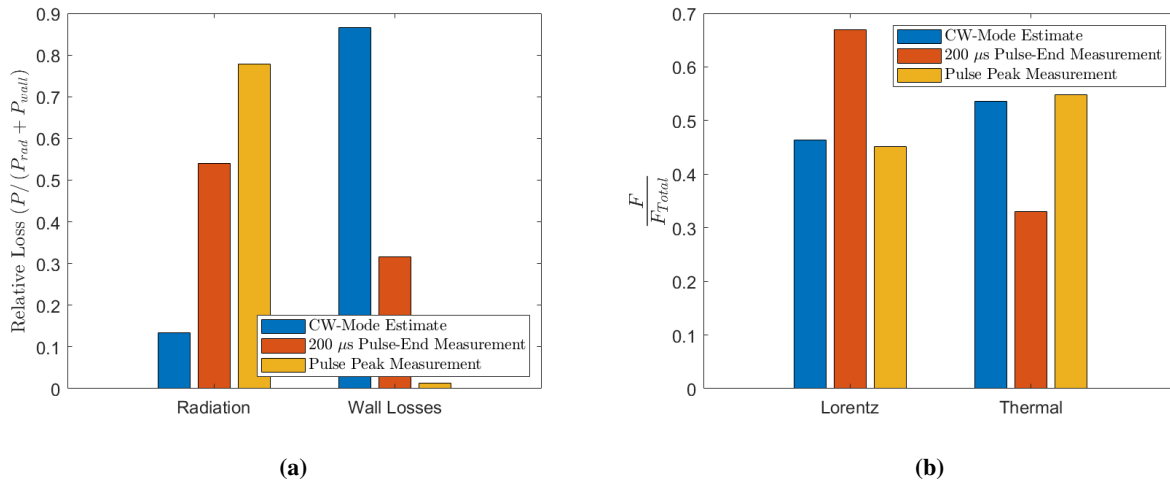


Fig. 6 Comparison of predicted a) loss mechanisms and b) force mechanisms for the 45 sccm, 180 G bias field condition. Pulsed-mode operation for which the data was taken used 2000 A pk-pk RMF current.

With this being said, the issue of low efficiency is clearly not solved by the switch to CW-mode operation, as the wall losses have become significant where they were not during pulsed operation. To consider why this might be the case, we can refer to the relative scaling for jet power, radiated power, and wall losses discussed in Section V. We observe that jet power will scale quadratically with electron density, as will radiation losses. Wall losses, meanwhile, only scale linearly. Therefore the radiation losses are reduced commensurately with jet power, while wall losses are mitigated to a significantly lesser degree.

To contextualize the power loss terms with respect to the forces, we look to Figure 6b, where we can see that thermal forces are commensurate with Lorentz forces, and are larger for both the pulse peak and CW-mode prediction. The thruster in its present state is therefore behaving as a mostly thermal device, despite all design work geared toward the Lorentz force being the chief driver of momentum transfer to the propellant. In light of the fact that this thermal thrust is due to electron thermal pressure on the physical walls of the device, it is not surprising that electron wall losses are dominant.

VII. Discussion

A. Scaling consequences

These results point to the conclusion that CW-mode operation of the RMFv2 thruster, while anticipated to be significantly more performant than pulsed operation, is still not an effective method of thrust generation due to high power losses. While in pulsed operation, radiation losses dominate with electron wall losses accounting for a small fraction of power lost, the situation is expected to reverse for CW-mode operation. Additionally, the CW-mode RMF thruster in its present configuration is predicted to behave fundamentally as a thermal thrust device, but without the design optimization for such behavior.

According to the equations set forth in Section V, increasing the power level of the device ought to be possible by increasing the mass flow rate and maintaining similar penetration. Jet power will increase quadratically with density, as both Lorentz force and electron pressure increase linearly with density. Radiation losses, while insignificant at the densities associated with CW-operation at the mass flow rates considered in this study, also increase quadratically with

density. Wall losses, the dominant loss mechanism for the cases considered, increase only linearly as density increases. Therefore, we may expect an optimum mass flow rate for CW-mode operation of the RMF thruster in which radiation and wall losses are balanced. The ~ 4 times higher performance calculated for the 200 μs pulse-end condition, in which the two plasma losses are much closer to each other in magnitude, provides some evidence for this claim.

B. Mitigation Strategies

Due to the scaling relations set forth, few parameters exist which appear to significantly change performance. As a result, fundamental changes should be made to the device if we wish to improve the efficiency by means of loss mechanism reduction. While the coupling efficiency η_c is significantly greater than the plasma and acceleration efficiency $\eta_a\eta_p$, it still accounts for a large amount of power lost. Indeed, the line losses P_{LL} represent the single largest loss mechanism in terms of raw magnitude. Therefore a re-examination of the switching circuitry used in the RMFv2 thruster is warranted before attempting CW-mode operation. Larger conductors and more efficient switches could serve to significantly reduce this loss mechanism. The line losses could also be reduced by further reduction in RMF current. In this analysis we make the assumption that the penetration condition remains the same between the pulsed and CW-mode operation. However, we do not presently have a clear understanding on when penetration is truly lost owing to the 'much greater than' condition present in Eqn. 12. Therefore, it may be possible to reduce the RMF current without causing significant reduction in jet power, enabling a reduction in P_{LL} quadratic with the reduction in input current.

To reduce the losses which happen in the plasma itself, a re-examination of the bias magnetic field is warranted. In particular any change in magnetic field which might reduce electron-wall interaction could reduce the electron wall loss term. A study into the shape of the bias magnetic field could prove valuable in this respect. While such a change would also reduce the thermal component of force as calculated in this analysis, we posit that a more effective magnetic field would translate the electron energy into current via the diamagnetic drift, which would then appear in the Lorentz force term as additional current.

C. Analysis Shortcomings

This analysis requires several large assumptions which must be kept in mind when discussing its conclusions. First among these is the stipulation that neutral density, electron density, current density, and electron temperature profiles are conserved between the pulsed and CW-mode operation. Because of the nature of the two conditions, this assumption is likely inaccurate. The density profile in the pulsed case is measured shortly after the ionization of neutrals whose distribution will be determined by thermal diffusion at a constant thermal velocity. In contrast, the velocity of ions in CW-mode can realistically be expected to vary throughout the cone as it is accelerated, likely through some finite acceleration region. This would lead to very different shape of the density profile. Evidence for this being the case can be found by comparing the shape of the total integrated electron number found in Figure 5 to the total current for the 200 μs pulse. While the shapes of the two curves match remarkably well until the ~ 150 μs point, they deviate significantly after, invalidating the assumption that the current density and electron density share the same profile at all times. Additionally, because several terms depend on the density profile (in particular the wall losses and thermal force which depend on the density along the thruster wall and the current density, which in the ideal case is proportional to nr) the shape of this profile could have a large impact on the results. However, intuiting whether this effect would cause this analysis to over- or under-predict performance is not straightforward.

The next critical assumption is that the effective line resistance R_{eff} is constant between the vacuum shots calculated during the course of our completed measurements is constant at the lower CW-mode RMF currents. Because switching losses due to the IGBT switches employed in our power processing unit are not linear with current, the R_{eff} used in this analysis may be higher than the true value, which would serve to reduce the line losses. Proper characterization would require measurement in a representative test setup.

Finally, this analysis depends on quantities with non-negligible uncertainty – in particular the triple Langmuir probe analysis process, which is described in greater detail in Gill et al., 2022 [14]. As a result, while this analysis is useful for examining trends, data should not be expected to reproduce thruster behavior exactly.

VIII. Conclusion

In this study, we have applied analytic conservation and scaling arguments to experimental results for electron density and temperature and current density taken during pulsed operation of the RMFv2 thruster to attempt to predict performance during CW-mode operation. Thrust, specific impulse, power, and loss mechanisms are calculated across

three operating setpoints, including 45 sccm Xe/120 G centerline bias field, 45 sccm/180 G, and 60 sccm/180 G, at all of which the pk-pk current injected into the RMF antennas was 2 kA. Efficiency is predicted to increase by a factor of 3-5 times for all three setpoints, but overall efficiency still remains low at less than 2%, indicating that operating this device in CW-mode without more dramatic changes to its design will not be an effective method of thrust generation. By examining the various loss and acceleration mechanisms present in the device, we conclude that effort is likely warranted toward bias field optimization and reduction of losses inside the power processing unit itself.

Acknowledgments

We would like to acknowledge NSTRF Grant # 80NSSC18K1190 and NSTGRO Grant # 80NSSC20K1168 which supported this work. The power supply was developed as part of an SBIR award with Eagle Harbor Technologies, and additional funding was granted by AFOSR Grant FA9550-19-1-0022 from the Space Propulsion and Power portfolio.

References

- [1] Polzin, K., Martin, A., Little, J., Promislow, C., Jorns, B., and Woods, J., "State-of-the-Art and Advancement Paths for Inductive Pulsed Plasma Thrusters," *Aerospace*, Vol. 7, No. 8, 2020, p. 105.
- [2] "National Academies of Sciences Engineering and Medicine", *Space Nuclear Propulsion for Human Mars Exploration*, The National Academies Press, Washington, DC, 2021. <https://doi.org/10.17226/25977>, URL <https://www.nap.edu/catalog/25977/space-nuclear-propulsion-for-human-mars-exploration>.
- [3] Vitug, E., "Lunar Surface Innovation Initiative (LSII)," , Jul 2020. URL https://www.nasa.gov/directorates/spacetech/game_changing_development/LSII.
- [4] Blevin, H. A., and Thonemann, P. C., "Plasma confinement using an alternating magnetic field," *Nuclear Fusion Supplement, Part 1*, 1962, p. 55.
- [5] Jahn, R. G., *Physics of Electric Propulsion*, McGraw-Hill Book Company, New York, 1968.
- [6] Slough, J., Kirtley, D., and Weber, T., "Pulsed plasmoid propulsion: The ELF thruster," *31th International Electric Propulsion Conference*, 2009, pp. 20–24.
- [7] Weber, T. E., "The Electrodeless Lorentz Force Thruster Experiment," Ph.D. thesis, University of Washington, 2010.
- [8] Kirtley, D., Pancotti, A., Slough, J., and Pihl, C., "Steady operation of an FRC thruster on Martian atmosphere and liquid water propellants," *48th AIAA/ASME/SAE/ASEE Joint Propulsion Conference & Exhibit*, 2012, p. 4071.
- [9] Furukawa, T., Takizawa, K., Kuwahara, D., and Shinohara, S., "Electrodeless plasma acceleration system using rotating magnetic field method," *AIP Advances*, Vol. 7, No. 11, 2017, p. 115204.
- [10] Furukawa, T., Takizawa, K., Yano, K., Kuwahara, D., and Shinohara, S., "Spatial measurement in rotating magnetic field plasma acceleration method by using two-dimensional scanning instrument and thrust stand," *Review of Scientific Instruments*, Vol. 89, No. 4, 2018, p. 043505.
- [11] Furukawa, T., Shimura, K., Kuwahara, D., and Shinohara, S., "Verification of azimuthal current generation employing a rotating magnetic field plasma acceleration method in an open magnetic field configuration," *Physics of Plasmas*, Vol. 26, No. 3, 2019, p. 033505.
- [12] Sercel, C. L., Gill, T., Woods, J. M., and Jorns, B., "Performance Measurements of a 5 kW-Class Rotating Magnetic Field Thruster," *AIAA Propulsion and Energy 2021 Forum*, 2021, p. 3384.
- [13] Gill, T., Sercel, C. L., Woods, J. M., and Jorns, B. A., "Experimental Characterization of Efficiency Modes in a Rotating Magnetic Field Thruster," *AIAA SCITECH 2022 Forum*, 2022, p. 2191.
- [14] Gill, T. M., Sercel, C. L., and Jorns, B. A., "Experimental Investigation into Mechanisms for Energy Loss in a Rotating Magnetic Field Thruster," *37th International Electric Propulsion Conference*, 2022, pp. IEPC–2022–554.
- [15] Sercel, C. L., Gill, T. M., and Jorns, B. A., "Inductive Probe Measurements During Plasmoid Acceleration in an RMF Thruster," *37th International Electric Propulsion Conference*, 2022, pp. IEPC–2022–554.
- [16] Goebel, D. M., and Katz, I., *Fundamentals of Electric Propulsion: Ion and Hall Thruster*, Jet Propulsion Laboratory, California Institute of Technology, 2008.

- [17] Jones, I. R., and Hugrass, W. N., "Steady-state solutions for the penetration of a rotating magnetic field into a plasma column," *Journal of Plasma Physics*, Vol. 26, No. 3, 1981, pp. 441–453.
- [18] Viges, E. A., Jorns, B. A., Gallimore, A. D., and Sheehan, J., "University of Michigan's Upgraded Large Vacuum Test Facility," *36th International Electric Propulsion Conference*, 2019.
- [19] Dankanich, J. W., Walker, M., Swiatek, M. W., and Yim, J. T., "Recommended practice for pressure measurement and calculation of effective pumping speed in electric propulsion testing," *Journal of Propulsion and Power*, Vol. 33, No. 3, 2017, pp. 668–680.
- [20] Mikellides, I., Katz, I., Mandell, M., and Snyder, J., "A 1-D model of the Hall-effect thruster with an exhaust region," *37th Joint Propulsion Conference and Exhibit*, 2001, p. 3505.
- [21] Hayashi, M., "Luminous layers in the prebreakdown region of low pressure noble gases," *Journal of Physics D: Applied Physics*, Vol. 15, No. 8, 1982, p. 1411.
- [22] Hayashi, M., "Determination of electron-xenon total excitation cross-sections, from threshold to 100 eV, from experimental values of Townsend's α ," *Journal of Physics D: Applied Physics*, Vol. 16, No. 4, 1983, p. 581.